mito-QC illuminates mitophagy and mitochondrial architecture in vivo

Thomas G. McWilliams,[1] Alan R. Prescott,[2,3] George F.G. Allen,[1] Jevgenia Tamjar,[1] Michael J. Munson,[1] Calum Thomson,[3] Miratul M.K. Muqit,[1,4] and Ian G. Ganley[1]

[1]Medical Research Council Protein Phosphorylation and Ubiquitylation Unit, [2]Division of Cell Signalling and Immunology, [3]Dundee Imaging Facility, School of Life Sciences, and [4]School of Medicine, University of Dundee, Dundee DD1 9SY, Scotland, UK

Autophagic turnover of mitochondria, termed mitophagy, is proposed to be an essential quality-control (QC) mechanism of pathophysiological relevance in mammals. However, if and how mitophagy proceeds within specific cellular subtypes in vivo remains unclear, largely because of a lack of tractable tools and models. To address this, we have developed "*mito*-QC," a transgenic mouse with a pH-sensitive fluorescent mitochondrial signal. This allows the assessment of mitophagy and mitochondrial architecture in vivo. Using confocal microscopy, we demonstrate that *mito*-QC is compatible with classical and contemporary techniques in histochemistry and allows unambiguous in vivo detection of mitophagy and mitochondrial morphology at single-cell resolution within multiple organ systems. Strikingly, our model uncovers highly enriched and differential zones of mitophagy in the developing heart and within specific cells of the adult kidney. *mito*-QC is an experimentally advantageous tool of broad relevance to cell biology researchers within both discovery-based and translational research communities.

Introduction

Damaged mitochondria have a deleterious impact on cellular metabolism, promote the production of reactive oxygen species, and ultimately trigger apoptosis (Nunnari and Suomalainen, 2012; Wang and Hekimi, 2015). Removal of such mitochondria is therefore essential to prevent cellular dysfunction, and this is believed to occur primarily through autophagy. Mitochondrial autophagy or mitophagy, involves the sensing, sequestration, and trafficking of damaged mitochondria to the lysosome for degradation. Over the past decade, a complex picture of mitophagy has emerged, revealing multiple signaling pathways and routes by which mitochondria can be delivered to lysosomes (Youle and Narendra, 2011; Wei et al., 2015; Yoshii and Mizushima, 2015). These discoveries have relied on the induction of mitophagy by treating cultured cell lines with cytotoxic mitochondrial uncoupling or damaging agents. Although informative for molecular studies of stress-induced mitophagy in vitro, it has been difficult to reconcile analogous physiological scenarios under which such mitophagy pathways may operate in vivo. As a result, there exists a paucity of data on the physiological relevance and nature of vertebrate mitophagy.

Current methods to visualize mitochondrial turnover in mammalian tissues include the following:

(1) Electron microscopy. This method visualizes mitochondria surrounded by autophagic/lysosomal membranes and provides rigorous detection of mitophagy. However, this is time consuming and requires an expert eye for accurate quantification, and it is often challenging to identify specific cell types with confidence in heterogeneous tissues.

(2) Measuring lysosomal-sensitive loss of mitochondrial proteins biochemically (e.g., immunoblotting or citrate synthase activity assay). This approach cannot distinguish between different cell types within a tissue, and the low sensitivity of currently available biochemical methods relies upon a high degree of mitophagy for accurate measurement. Additionally, lysosomal inhibitors required for these assays can have secondary effects and are not well tolerated in animals for in vivo studies.

(3) Immunofluorescence-based colocalization of mitochondria with autophagosomes or lysosomes. This cannot accurately distinguish between autophagy and mitophagy, as general nonspecific autophagosomes likely form at mitochondria (Hailey et al., 2010; Hamasaki et al., 2013). In addition, sensitive and specific antibody staining is needed, as well as careful tissue processing to preserve epitopes yet allow tissue penetration of antibodies.

(4) Ratiometric fluorescence probes. mt-Keima is a pH-sensitive fluorescent protein targeted to the mitochondrial matrix that has been successfully used to study mitophagy in vitro (Katayama et al., 2011; Bingol et al., 2014). Recently, Sun

Correspondence to Ian G. Ganley: i.ganley@dundee.ac.uk

Abbreviations used: AR, antigen retrieval; DCT, distal convoluted tubule; E, embryonic day; MEF, mouse embryonic fibroblast; OMM, outer mitochondrial membrane; PCT, proximal convoluted tubule; QC, quality control; RMCE, recombination-mediated cassette exchange; WT, wild type.

The Rockefeller University Press $30.00
J. Cell Biol. Vol. 214 No. 3 333–345
www.jcb.org/cgi/doi/10.1083/jcb.201603039

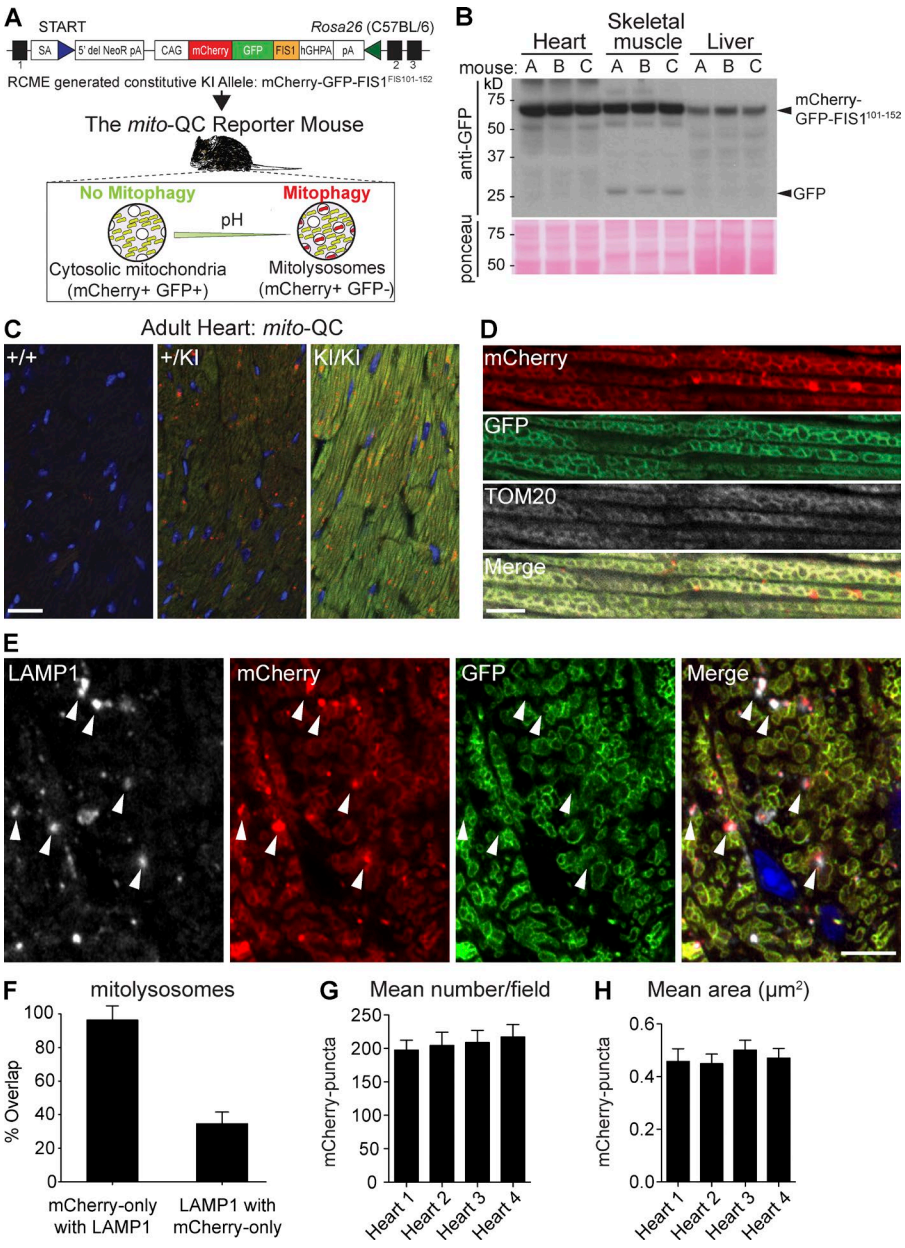

Figure 1. **Generation of the *mito*-QC mouse and detection of mitophagy and mitochondrial architecture in vivo.** (A) Schematic of gene targeting strategy used to generate the *mito*-QC mouse model. (B) Representative anti-GFP immunoblot showing expression of the reporter construct in different tissues from heterozygous reporter mice (designated A, B, and C). Ponceau is shown to indicate protein loading. (C) Sections of adult heart isolated from *mito*-QC littermate mice. Images depict representative heart sections from animals with and without indicated copies of the reporter construct. DAPI nuclear stain shown in blue. Bar, 20 µm. (D) Images of *mito*-QC heart tissue sections immunolabeled with antibodies to the mitochondrial marker, TOM20. Bar, 5 µm. (E) *mito*-QC heart tissue sections immunolabeled with antibodies to the lysosomal marker LAMP1. Bar, 5 µm. Arrowheads indicate examples of LAMP1/mCherry-only (GFP-negative) colocalization. (F) Quantification of mCherry-positive mitolysosomes in heart sections obtained from homozygous *mito*-QC adult littermate mice (n = 4 mice). (G) Quantification of mean mitolysosome size between *mito*-QC adult littermate mice (n = 4 mice). (H) Quantitation of mean cardiac mitolysosome area in *mito*-QC adult littermate mice (n = 4 mice). Error bars in F–H depict standard deviation.

et al. (2015) described the mt-Keima mouse, based on the same precept. Although Sun et al. (2015) reported the occurrence of basal mitophagy in tissue sections, the utility of mt-Keima in tissues has considerable limitations. The Keima protein is incompatible with fixation and can also exhibit spectral overlap. Thus, it is infeasible to investigate mitophagy with precision and resolve mitochondrial morphology within immunochemically labeled cellular subtypes in vivo.

To circumvent these problems, we took advantage of a binary-based fluorescence assay previously developed in our laboratory (Allen et al., 2013). This assay is based on the expression of a functionally inert, tandem mCherry-GFP tag fused to the mitochondrial targeting sequence of the outer mitochondrial membrane (OMM) protein, FIS1 (comprising amino acids 101–152). Under steady-state conditions, the mitochondrial network fluoresces both red and green; however, upon mitophagy, mitochondria are delivered to lysosomes where mCherry fluorescence remains stable, but GFP fluorescence becomes quenched by the acidic microenvironment. This results in the appearance of punctate mCherry-only foci that can be easily quantified as an index of cellular mitophagy. Therefore, to address the challenge of resolving mitochondrial network architecture and mitophagy in vivo, we have exploited this end-point assay approach by generating a transgenic mouse model, which we have called *mito*-QC, to highlight its use in monitoring mitochondrial quality control (Fig. 1 A). Given the essential energy-generating function of mitochondria, we chose to use *mito*-QC to investigate mitochondrial turnover and organization in a range of metabolically demanding tissues. In the data presented, we reveal striking and hitherto unknown incidences of mitophagy in both the developing and mature heart and kidney. Additionally, we demonstrate its use as a tool to reveal the diversity of mitochondrial organization in specific subsets of cells within tissues of vital metabolic importance to mammals.

Results

Generation of a reporter mouse to visualize mitochondrial turnover and architecture in vivo

We exploited our previously published mitophagy assay to generate a transgenic reporter mouse (Allen et al., 2013). Targeted transgenesis was used to create *mito*-QC through constitutive knockin of mCherry-GFP-FIS1$^{101-152}$ (*mito*-QC) in the mouse *Rosa26* locus in the C57BL/6 background (Fig. 1 A). Expression from the *Rosa26* locus enables the ubiquitous spatiotemporal expression of our construct in all mammalian tissues (Soriano, 1999). Heterozygous and homozygous *mito-QC* mice appear healthy, and offspring are produced in accordance with expected Mendelian ratios, implying that the reporter knockin does not perturb mitochondrial function. In support of this, we found no differences in oxygen consumption between isolated wild-type (WT) versus heterozygous embryonic fibroblasts or WT versus heterozygous versus homozygous adult fibroblasts (Fig. S1, A and B). Additionally, mitochondrial morphology and dynamics appeared identical in wild type and littermate primary mouse embryonic fibroblasts (MEFs) as visualized by MitoTracker staining (Video 1). As a first step in validation, we confirmed that mitophagy could be induced in primary MEFs derived from *mito*-QC reporter embryos. In agreement with our previous study in reporter cell lines (Allen et al., 2013), we found that treatment with deferiprone, an iron chelator and potent mitophagy inducer, resulted in a sixfold increase in mitophagy over control cells, confirming that the assay is behaving as expected at the cellular level (Fig. S1, C and D). Also in agreement with our earlier study, immunofluorescence and immunoblotting assays revealed that stimulation of nonspecific autophagy, through inhibition of mTOR with the highly specific compound AZD8055 (in combination with bafilomycin A1 for biochemical experiments; Chresta et al., 2010), did not stimulate mitophagy, confirming the selective nature of our assay for mitophagy, but not general autophagy (Fig. S1, C and D). We were also able to show that primary WT and heterozygous MEFs displayed no significant difference in citrate synthase activity, a biochemical measurement of mitochondrial mass, either under basal or mitophagy stimulated conditions (Fig. S1 E).

Next, we analyzed expression of the reporter in heart, skeletal muscle, and liver by Western blot (Fig. 1 B). Using tissues isolated from three adult reporter mice, we detected a band corresponding to the predicted size of full-length *mito*-QC. Importantly, the expression of the reporter in each tissue is consistent between individual mice; however, we noted some variation in *mito*-QC transgene expression between tissues. Although the mitochondrial content of the tissue may account for this, we cannot exclude variations in transgene expression from the *Rosa26* locus. Regardless, only one major band is detected, indicating that *mito-QC* is stable and not subject to any overt cleavage. Intriguingly, a minor band corresponding to the size of free GFP was detected in skeletal muscle tissue. This may provide a readout of mitophagy, as the cleavage and lysosomal accumulation of GFP from GFP-tagged autophagosomal cargo proteins has been used as evidence for autophagy (Klionsky et al., 2016). In support of this, we have found skeletal muscle to have a high rate of mitophagy, based on *mito-QC* fluorescence (see the following section); however, further work is needed to confirm if the free GFP observed by Western blot is indeed a robust indication of mitophagy.

To assess if we could observe mitochondrial turnover and architecture in vivo, we examined tissue sections obtained from WT, heterozygous, and homozygous *mito*-QC littermate mice. As the intimate relationship between mitochondrial and cardiac function is well established (Dorn et al., 2015), we inspected cryosections of adult heart using conventional laser-scanning confocal microscopy. Although WT littermates exhibited no discernable GFP or mCherry signal, the architecture of the cardiac mitochondrial network was clearly visible in heart sections derived from littermate mice positive for the *mito*-QC reporter construct (Fig. 1 C). Moreover, mCherry-only (GFP-negative) puncta were visible in reporter heart sections, indicating the presence of degraded mitochondria in lysosomes. Although the fluorescence signal was greater in homozygous reporter mice than in their heterozygous siblings, the endogenous heterozygous signal was sufficient to observe both individual mitochondrial architecture and mCherry-only puncta using conventional confocal microscopy (Fig. 1 C). Considerable validation of this probe has been conducted in our previous cell-based study, yet we still sought to verify the mitochondrial and lysosomal signals in the reporter mice. To confirm the mitochondrial origin of the mCherry and GFP signals, we performed immunohistochemical labeling of reporter heart sections with antibodies to the OMM protein, TOM20. Immunolabeling revealed near-identical overlap with the pattern of the outer membrane reporter, verifying the mitochondrial localization of our reporter signal along with the characteristic morphology of cardiomyocyte mitochondria (Fig. 1 D). The mitochondrial localization of *mito*-QC relies on the targeting sequence of FIS1; however, FIS1 has been reported to also localize to peroxisomes (Koch et al., 2005). Thus, we assessed if *mito*-QC might also label peroxisomes. Immunohistochemical and immunocytochemical analyses using the peroxisomal marker anti-PMP70 revealed peroxisomes in close proximity to mitochondria. However, peroxisomal labeling displayed a distinct pattern to that of mitochondria in both *mito*-QC heart sections and isolated primary MEFs, demonstrating the selective labeling of *mito*-QC for mitochondria (Fig. S2, A and B). To validate that the mCherry-only puncta are in fact mitolysosomes, i.e., degraded mitochondrial components within lysosomes, we performed immunolabeling with antibodies to the lysosomal marker protein LAMP1. Quantitation of LAMP1 and mCherry-only signal revealed a 96% overlap in signals (Fig. 1, E and F). Almost all mCherry-only puncta are resident in LAMP1-positive lysosomes, yet analyses using our model also revealed that approximately one third of the LAMP1-positive network in the mammalian adult heart contains remnants of the degraded mitochondrial network (Fig. 1, E and F). Similarly, we were also able to detect LC3 colocalization with mCherry-only puncta, further confirming that these structures are autolysosomal in nature (Fig. S2 C). Additionally, levels of cardiomitophagy were comparable across multiple animals, as were the size of mitolysosomes (Fig. 1 G and H).

To further verify that *mito*-QC was selectively labeling mitochondria in vivo, we performed ultrastructural analyses of *mito*-QC tissues using cryo immunogold transmission EM. Immunolabeling of ultrathin heart tissue cryosections with gold-conjugated anti-GFP antibodies revealed a clear (90%) overlap of the label with mitochondria (Fig. S3, A and B). Thus, data from both light and electron microscopy studies demonstrate the exclusivity of the *mito*-QC signal for mitochondria in vivo. Although our cryolabeling methods successfully revealed GFP labeling with a high signal to noise ratio in reporter tissue

samples, it did not preserve membrane architecture sufficiently to unambiguously detect gold-labeled mitochondria in autophagosomes. Nonetheless, presumptive mitophagosomes identified in heart EM cryosections compared well to mitophagosomes identified using conventional resin-embedded transmission EM, which afforded superior membrane preservation (compare the top and bottom panels in Fig. S3 C). Further EM examples of cardiac mitochondria engulfed by the characteristic autophagic double lipid bilayer are shown in Fig. S4 (B and C). Importantly, comparative assessment of heart resin-embedded sections from WT and reporter littermates revealed no apparent differences in mitochondrial morphology by transmission EM (Fig. S4 A). This demonstrates that the genetically encoded OMM tag has no deleterious effects on mitochondrial morphology in vivo. Collectively, our converging analyses demonstrate the utility of the *mito*-QC model to reveal mitochondrial architecture and mitophagy in vivo. Furthermore, *mito*-QC demonstrates mitophagy to be a constitutive process in the mature heart under steady-state conditions in mammals.

Developmental cardiomitophagy and diverse mitochondrial morphology revealed by *mito*-QC

Mitophagy is clearly evident in the adult mouse heart, but less is known about mitochondrial turnover and the organization of mitochondrial networks during cardiac development. Therefore, we sought to exploit *mito*-QC to investigate mitophagy during embryonic development, shortly after cardiomyocytes become defined. Fig. 2 shows micrographs of the heart at embryonic day 14.5 (E14.5; Fig. 2 A), E17.5 (Fig. 2 B), and adult stages (Fig. 2 C). Investigation of mitophagy at E14.5 revealed that considerably less turnover occurs at this period in development, relative to observable levels in the adult (Fig. 2, A and C). After E17.5, however, we observed restricted cellular zones in the embryonic heart undergoing mitophagy (see arrows in Fig. 2 B), which was in contrast to the lower but uniformly distributed mitophagy observed in the adult heart (highlighted in Fig. 2, D and E). These restricted zones were stochastically distributed and characterized by a dense cellularity possibly indicating tissue remodelling (compare DAPI staining in Fig. 2, F and G). To gain insight into this localized mitophagy, we assessed if these cells were undergoing developmental apoptosis or cell proliferation. To monitor apoptosis, we performed immunohistochemistry to activated caspase-3, an established marker of dying cells. As this stage in development is beyond the defined period of active programmed cell death (Barbosky et al., 2006), we observed low immunoreactivity for caspase-3 in the heart and no overlap with cells undergoing mitophagy (Fig. 2 F). To determine if these cells might be dividing or cycling, we assayed embryonic heart sections with antibodies to the proliferative marker, Ki67. Our findings showed a mutual exclusion of Ki67-positive cells and mitophagic cells in the E17.5 heart (Fig. 2 G). Therefore, these highly mitophagic cells appear not to be dying or proliferating, suggesting that they are undergoing remodelling or differentiation. Interestingly, a recent publication has proposed that perinatal cardiomyocytes undergo mitophagy to repopulate the network with mitochondria that are optimized for fatty acid metabolism (Gong et al., 2015). Our observations imply that this transformation may commence at a much earlier developmental stage. Regardless, our findings clearly demonstrate that cardiomitophagy is a developmentally regulated process in mammals.

In addition to mitophagy, *mito*-QC also allowed assessment of the mitochondrial network and revealed interesting differences in the organization of cardiac mitochondria, both within the same heart at E17.5 and when comparing this stage to the adult heart (Fig. 3). High-resolution Airyscan confocal imaging of E17.5 heart tissue revealed that the mitochondrial network of cells within mitophagic zones was disordered and greatly reduced in mass. Conversely, cells with reduced mitophagy exhibited highly organized mitochondria and a greater overall level of mitochondrial content (Fig. 3, A–C). We extended this comparative analysis to adult ventricular heart tissue and observed a highly ordered and stereotypical arrangement of individual mitochondria in defined chain-like networks along the muscle fibers (Fig. 3 D). Most adult cardiomyocytes exhibited a robust level of turnover, with no discernable reduction in mitochondrial mass or spatial restriction of mitophagic cells as we observed in the embryonic heart. For comparison, we also examined sections of adult skeletal muscle and the tongue. In skeletal muscle, we observed mitophagy to occur at a similar level to cardiac muscle (Fig. 3 E). Recently, a mitochondrial reticulum has been described here, and distinct types of mitochondria have been demonstrated with the aid of EM tomography (FIS-SIM [Glancy et al., 2015]). With *mito*-QC and conventional confocal microscopy, we were able to clearly observe these distinct structures. The mammalian tongue is a metabolically demanding muscular and gustatory organ, often affected in a variety of congenital and acquired disease states (Kutuzov and Sicher, 1953; Rajendran and Sivapathasundharam, 2009). Owing to its unique anatomy, histological tongue preparations facilitate the visualization of adjacent longitudinal and transverse muscle fibers within the same section. Although the macroanatomy of the tongue has been well established, little has been reported about the cell biology of mitochondrial networks within this tissue since classical EM studies in the 1950s (Wachstein and Meisel, 1955). Imaging of parasagittal tissue sections revealed a unique organization of mitochondria within the interwoven muscle fibers of the adult tongue (Fig. 3, F and G). Mitochondria were densely packed along the muscle fibers, and the network was both grid-like and expansive in arrangement. We were also able to detect distinct organizations of sarcolemmal mitochondria along individual longitudinal muscle fibers (Fig. 3 G). Interestingly, we observed a high degree of mitophagy in the muscle fibers of tongue, with mCherry-positive mitolysosomes situated at the periphery and more medially within the tubular arrangement of fibrils. We also observed a considerable degree of turnover at orthogonal intersections of muscle (Fig. 3 G, asterisks). Although it is known that multinucleated regions of tongue muscle fibers are enmeshed within dense mitochondrial networks (Sandborn, 1972), our model reveals for the first time that this is also a major site of mammalian mitophagy. This localization contrasts with our observations in adult cardiac and skeletal muscle, where mitochondria appear to be routinely eliminated without any discernable pattern.

mito-QC illuminates mitophagy in the nervous system

We next explored the suitability of *mito*-QC to investigate mitochondrial turnover in the vertebrate nervous system, another region of high metabolic demand. The maintenance of mitochondrial integrity here is receiving much attention as a burgeoning area of important research with respect to nervous system dysfunction (Carelli and Chan, 2014; Burté et al., 2015).

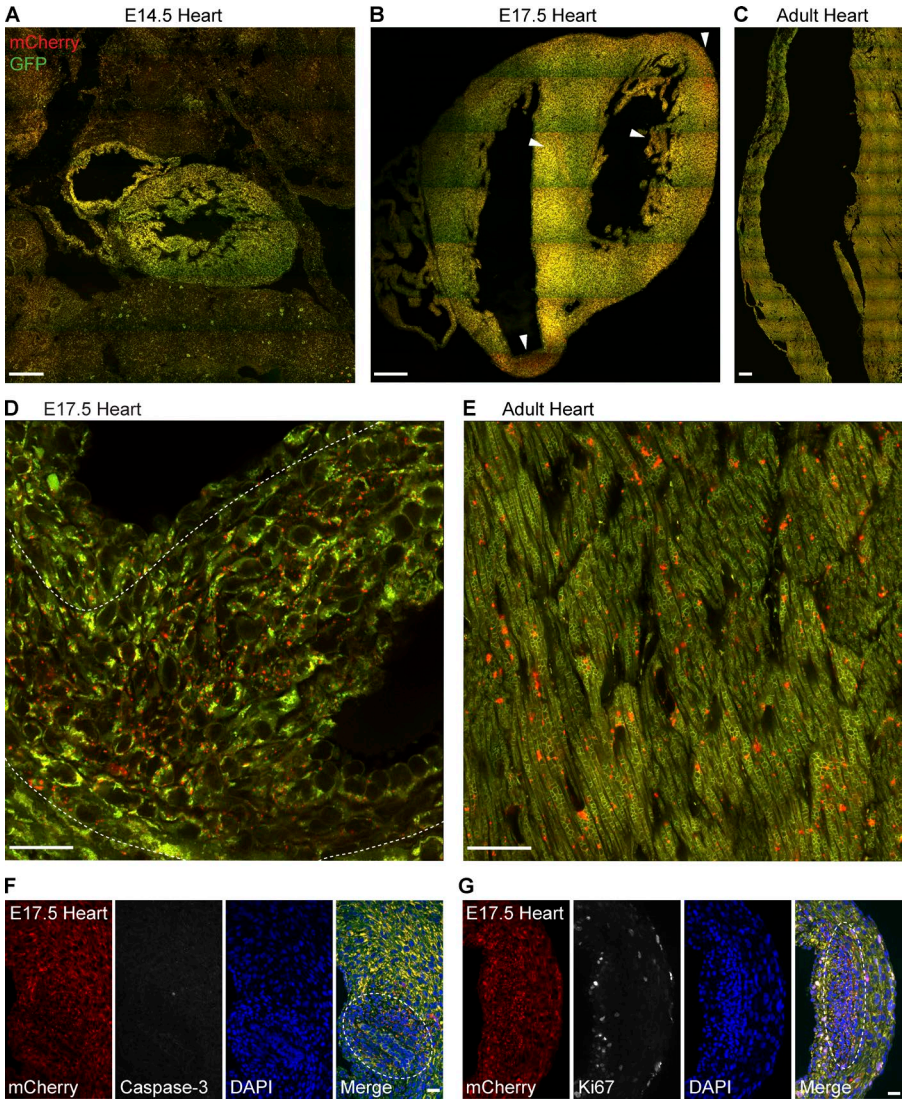

Figure 2. **Differential and zonal regulation of cardiomitophagy during development.** (A–C) Representative montage of tile-scan images of E14.5 (A), E17.5 (B), and adult heart (C) sections from *mito*-QC reporter mice. Arrowheads in B indicate areas of high mitophagy. As images are to scale, and only a representative sample of adult cardiac tissue is depicted in C. Bars, 200 µm. (D) High resolution Airyscan images showing a mitophagic zone (delineated by dotted line) in the E17.5 ventricle Bar, 20 µm. (E) Representative Airyscan image of adult ventricular cardiomyocytes in vivo. Bar, 20 µm. (F) Immunostaining of E17.5 heart sections with anti–activated caspase-3 antibodies. Dotted line highlights high mitophagic zone. Bar, 20 µm. (G) Immunostaining of E17.5 heart sections with anti-Ki67 antibodies. Dotted line highlights high mitophagic zone. Bar, 20 µm.

Protruding from the rostral hindbrain, the cerebellum is recognized as one of the most experimentally amenable systems in the mammalian CNS (Leto et al., 2015). The heterogeneity of cell types and connections in the cerebellum makes it an ideal region for comparative in vivo cell biology. We assessed parasagittal sections of adult cerebellum from *mito*-QC mice (Fig. 4). We observed the most pronounced mitolysosomes in the monolayer of somata between the molecular and granule cell layers, corresponding to the Purkinje cell layer. Purkinje cells are among the largest and most studied neurons in the adult CNS and are the sole output neurons of the cerebellar cortex. To validate our observations, we conducted immunohistochemical labeling with antibodies to calbindin-D28K, a classical marker of Purkinje neurons and their processes (Celio, 1990; Scotti, 1995). Immunolabeling of *mito*-QC sections confirmed our observations that Purkinje neurons undergo pronounced mitochondrial turnover (Fig. 4, A and B). Further investigation revealed minimal mitophagy in calbindin-positive dendritic arbors or axonal projections. Rather, it appears the majority of mitochondrial turnover occurs in the Purkinje somata, suggesting mitochondria, or mitolysosomes, may be transported to the cell body for final degradation. These observations are highlighted in Fig. S5 (A and B), which shows Purkinje mitochondria specifically. At higher magnifications, we were also able to resolve individual segments of the mitochondrial network within distinct neuronal compartments of Purkinje cells. In the proximal smooth shaft of the Purkinje dendritic field, we observed mitochondria at the process edges. Segments of the mitochondrial network were also observable at bifurcation points, in stretches of smaller dendritic arbors and in calbindin-negative fibers of nonneural cells (Fig. 4, C–F).

As we could successfully detect mitochondrial turnover and architecture within a subpopulation of neurons using conventional immunohistochemistry, we next probed the compatibility of *mito*-QC with a more contemporary immunohistochemical approach. iDISCO is a recently reported technological advance that enables volume imaging of large tissue specimens such as whole organs (Renier et al., 2014). We performed iDISCO on intact, hemisected cerebellum preparations from heterozygous *mito*-QC mice, labeled with antibodies to GFP and mCherry as per the published protocol. Although we encountered difficulties in resolving individual mitolysosomes in the cerebellum (likely because of the required labeling and harsh clearing treatments resulting in de-quenching of the GFP signal), we were able to visualize the spatial disposition of the mitochondrial network along neural projections, giving a

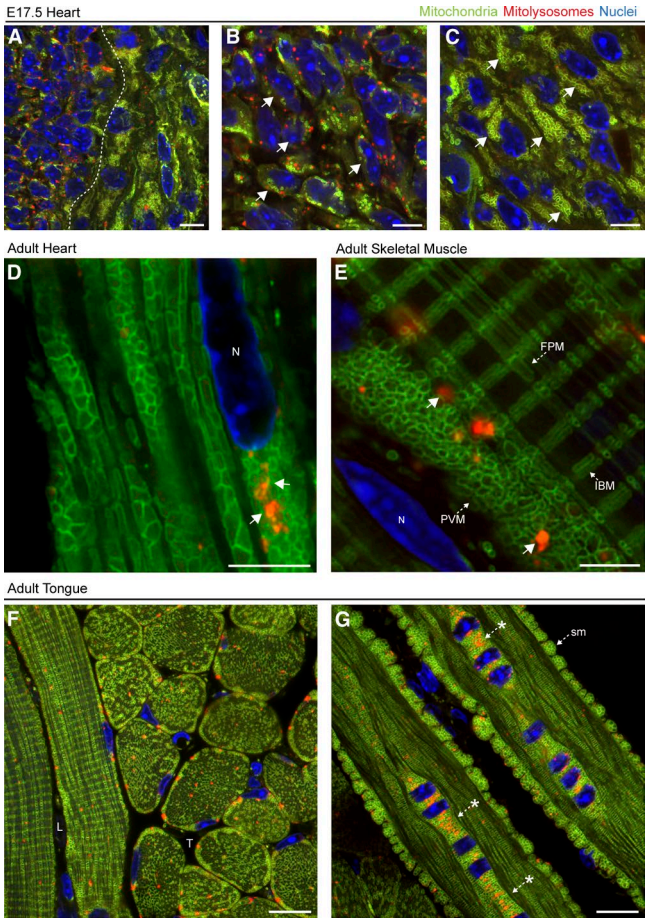

Figure 3. **Comparative overview of mitochondrial networks in developing and adult muscle tissues in vivo.** (A–C) High-resolution Airyscan images of E17.5 heart. Dotted line indicates division between high and low mitophagic regions. Magnified photomicrographs of mitochondrial architecture in regions with high and low degrees of mitophagy are shown in B and C, respectively. Arrows highlight the differential organization of mitochondrial networks within cells of the same tissue. (D) High-magnification Airyscan image of adult *mito*-QC heart, depicting the mitochondrial architecture and the position of mitolysosomes (arrows) within ventricular cardiomyocytes in vivo. N, Nucleus. (E) High-magnification Airyscan image of a mitochondrial network depicting mitolysosomes and aspects of the recently described mitochondrial reticulum within adult skeletal muscle. Arrows indicate different muscle mitochondrial morphologies. FPM, fiber parallel mitochondria; PVM, paraventricular mitochondria; IBM, I-band mitochondria. Bars, 5 µm. (F and G) Representative images from parasagittal sections of adult tongue from a *mito*-QC reporter mouse. Bars, 10 µm. (F) Image shows transverse (T) and longitudinal (L) fibrils containing mitochondrial networks and mitolysosomes. (G) Image of a longitudinal tongue muscle fiber with sarcolemmal (sm) mitochondria at the periphery of the fiber and a cluster of mitolysosomes at a multinucleated orthogonal intersection (asterisks). DAPI is shown in blue throughout.

powerful overview of the mitochondrial network at the regional level (Fig. S5 C and Video 2). Collectively, we predict that the *mito*-QC mouse holds significant potential to reveal insights about mitochondrial network biology under various pathophysiological conditions in the vertebrate nervous system in vivo.

mito-QC as a tractable tool to quantitate mitophagy in vivo

A major limitation of current models is their incompatibility with routine immunohistochemical approaches. We have demonstrated that *mito*-QC is fully compatible with a variety of labeling techniques, making it possible to investigate mitochondrial turnover and architecture within specific cell types in vivo with precision. We next explored if the model was amenable to quantitation and if this could be used to predict differences in the basal rates of mitophagy in vivo. We selected a range of typical organs used in routine pathological analysis and performed semiautomated quantitation on confocal photomicrographs from tissue sections (Fig. 5). It is important to note that our model facilitates a variety of analyses, depending on the research question of interest. Earlier, we demonstrated that levels of cardiomitophagy were consistent between different adult reporter animals (Fig. 1, F and G). Thus, we sought to compare global levels of steady-state mitophagy, as a proof-of-principle for our model. As described in Materials and methods, we devised a simple algorithm to quantify mitophagy by automated analysis. We specified mCherry-only mitolysosomes as unique objects and used the GFP signal to define the area of the tissue to be analyzed. In combination with sufficient fields and biological replicates as well as blinded analysis, we found it was possible to assay in vivo mitophagy in a generalized manner. Our results show that mitophagy occurs to a similar degree in heart and skeletal muscle, but to a lesser degree in the spleen (Fig. 5 D). Interestingly, we observed the highest levels of mitophagy in hepatic and renal tissue. A caveat of our example analysis is that no consideration is given to the identity of specific cell types within the tissues analyzed; however, given the compatibility of our model with immunohistochemistry (see examples in Fig. 1, D and E; Fig. 2, F and G; Fig. 4; and Fig. 6, C and D), quantitative analysis of mitophagy within cellular subpopulations is clearly possible.

The kidneys are a major site of mitophagy in mammals

As we observed pronounced mitochondrial turnover in the kidneys using our generalized screen, we performed a comprehensive analysis of renal mitophagy using the *mito*-QC mouse model. The kidneys are an important excretory organ and regulate vital functions such as water homeostasis, acid–base and electrolytic balance, arterial pressure, hormone metabolism, and gluconeogenesis (Fougeray and Pallet, 2015). This indispensable contribution to the maintenance of normal physiology makes the renal system a site of high metabolic demand in mammals. The nephron has been suggested as a clinically relevant site of mitochondrial turnover in mammals, yet experimental evidence for this has been lacking because of an absence of robust tools to demonstrate this (Higgins and Coughlan, 2014; Eirin et al., 2015). Conveniently, as with other tissues, we observed that the OMM localization of *mito*-QC in the kidneys facilitated identification of major anatomical landmarks using standard fluorescence microscopy. We observed a striking pattern of mitophagy across the adult kidney (Fig. 6 A), with the most pronounced mitochondrial turnover in tubules of the renal cortex (Fig. 6, A and B). Moreover, mitolysosomes displayed a distinct coronal-like and apical positioning within these tubule cross sections. To visualize the spatial disposition of mitochondrial turnover within the adult kidney at a whole-tissue level, we used an adapted version of the previously mentioned iDISCO method. By simply using the optical clearing steps of iDISCO, without antibody labeling, on fixed whole-kidney specimens combined with multiphoton confocal microscopy, we observed that mitophagy in the adult kidney is spatially restricted to particular

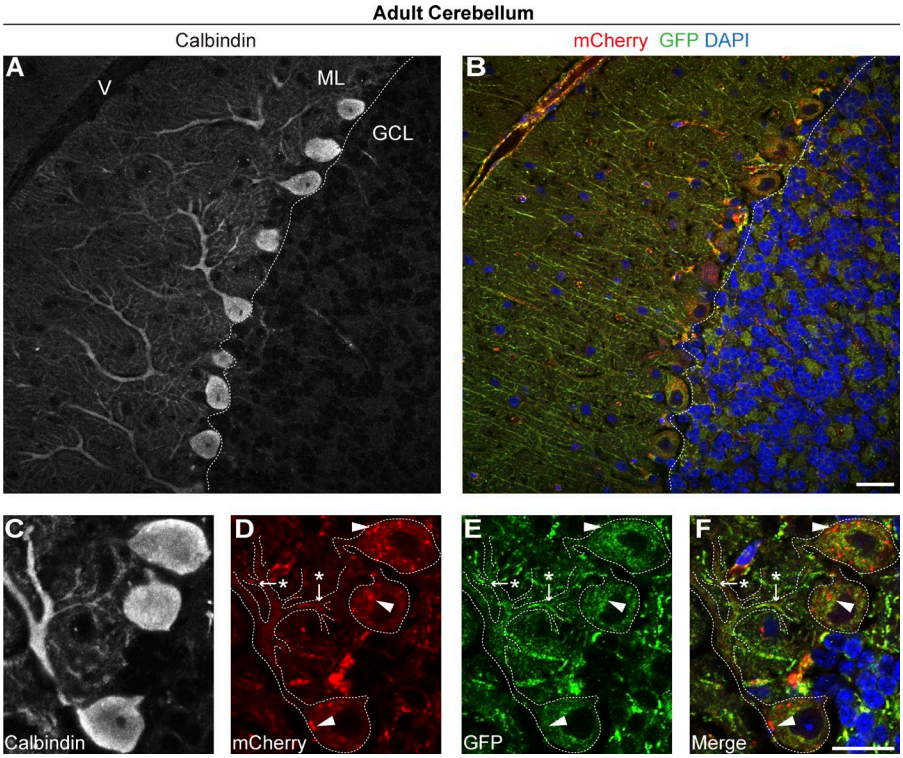

Figure 4. **Mitophagy and mitochondrial architecture in defined subsets of cerebellar neurons.** (A) Representative images from a parasagittal section of adult cerebellum from *mito*-QC reporter mouse, labeled with antibodies to the Purkinje neuron marker calbindin-D28K. ML, molecular layer; GCL, granule cell layer; V, vasculature. (B) Reporter signal in same immunolabeled region as A, with DAPI shown in blue. (C–F) Magnified view of a calbindin-positive Purkinje neuron in the cerebellum, with panels showing calbindin (C), mCherry (D), GFP (E), and merge (with DAPI; F). Dashed lines demarcate calbindin-positive neuronal processes, whereas arrows/asterisks highlight mitochondria (mCherry- and GFP-positive) situated at dendritic bifurcation points and arrowheads highlight examples of mitophagy (mCherry only) in the soma. Bars, 20 µm.

cortical tubule segments of varying length from under 50 µm to over 300 µm (Fig. 6 B and Video 3). To verify the lysosomal nature of these puncta, we performed immunohistochemical labeling with antibodies to LAMP1. As expected, mCherry-only puncta in cortical tubules colocalized with LAMP1 staining, revealing the rich apical endolysosomal network characteristic of tubular cells of the nephron (Fig. 6 C). The histological profile of these distinct and highly mitophagic tubules, including their diameter, cuboidal morphology, and extensive brush borders, suggested they are proximal convoluted tubules (PCTs). To rule out the morphologically similar distal convoluted tubules (DCTs), we labeled *mito*-QC kidney sections with an antibody to the sodium-chloride cotransporter NCC, whose expression is restricted to the early segments of the DCT (Subramanya and Ellison, 2014). NCC-positive distal tubules exhibited minimal mitochondrial turnover, strongly supporting the notion of the PCTs being highly mitophagic (Fig. 6 D). Semiquantitative analysis of mitophagy within cortical tubules confirmed the highly polarized nature of this mitochondrial turnover in vivo (Fig. 6 E). Our high-resolution imaging of renal cortex also revealed the elaborate GFP-positive mitochondrial networks characteristic of renal tubules. Although PCT and DCT cells are densely packed with mitochondria, our reporter staining revealed higher mitochondrial content in DCTs. This is in good agreement with previous work, further validating our model (Dørup, 1985). Our observations also dispel the notion that the degree of mitophagy is proportional to the mitochondrial mass of a cell, at least in the context of PCT and DCT mitophagy.

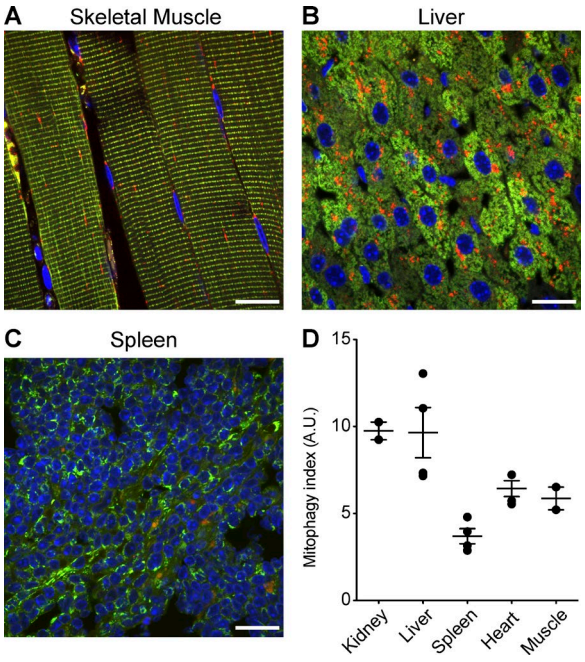

Figure 5. **Tissue-wide quantitation of mitophagy in vivo.** Representative images of skeletal muscle (A), liver (B), and spleen (C) used to perform generalized analysis of mammalian mitophagy across selected tissues in vivo. (D) Scatterplot depicting the mean relative level of global mitophagy in different organs in vivo, where each data point represents an organ from an individual animal and error bars represent standard error. Bars, 20 µm.

Spatiotemporal regulation of mitochondrial turnover in the mammalian kidney

Given our observations of mitophagy in the adult kidney, we next investigated the kidney at an earlier stage of development to perform a comparative assessment. Urine production in the mouse kidney begins during late gestation at E16.5 (Airik and Kispert, 2007), and thus, we investigated sections obtained from E17.5 reporter mouse kidneys. In contrast to the adult,

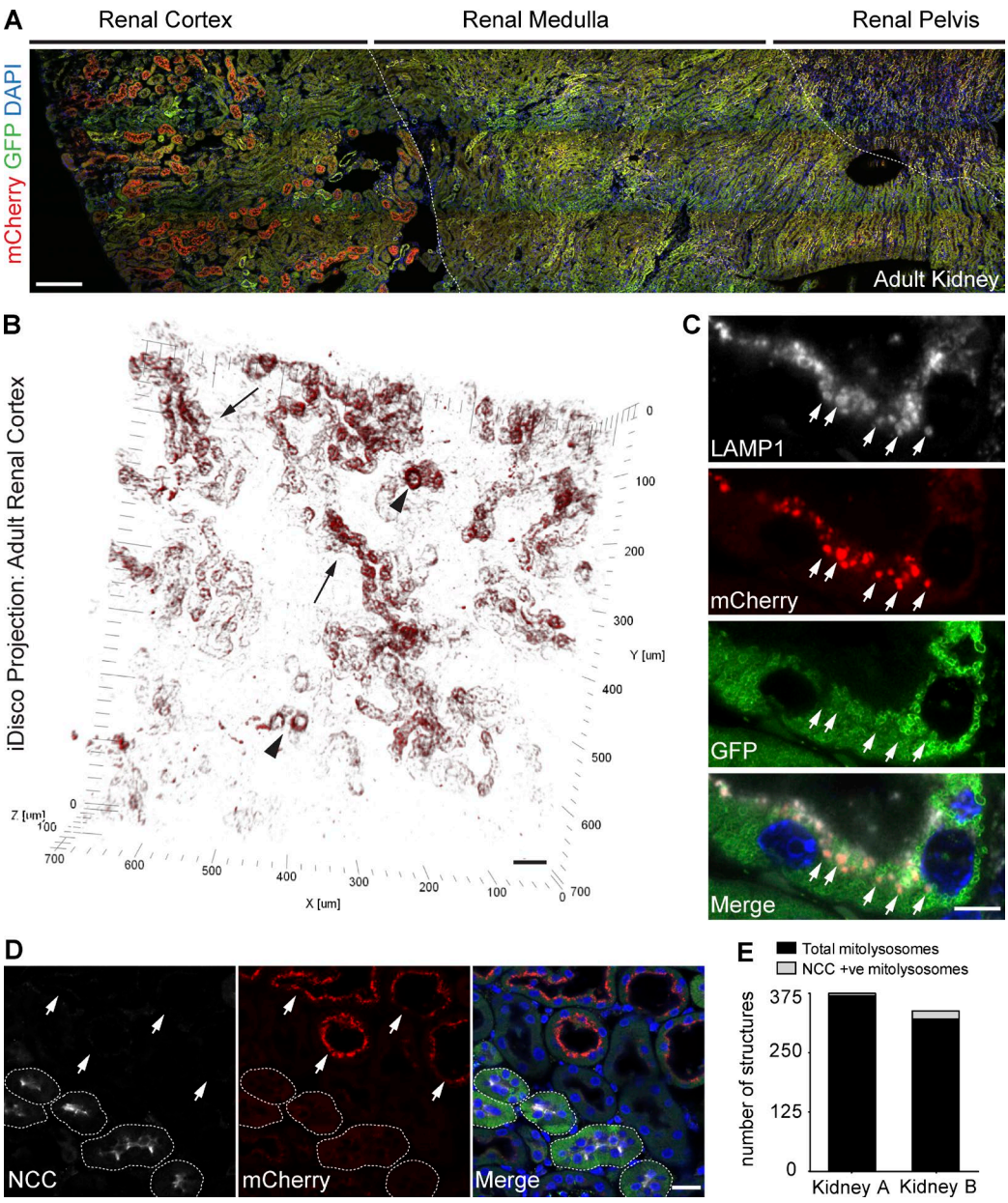

Figure 6. **The renal tubules are a major site of mammalian mitophagy in vivo.** (A) Tile scan showing parasagittal view of a representative adult kidney section from a *mito*-QC reporter mouse. Dashed lines demarcate macro-anatomical regions of the kidney, (lateral-medial from left-right). Bar, 200 µm. (B) 3D projection showing the spatial distribution of mitolysosomes within renal cortical tubules in vivo. Image acquired using iDISCO from an intact, cleared, and nonimmunolabeled *mito*-QC adult kidney with multiphoton microscopy. Arrows depict long stretches of cortical tubules with mitophagy, whereas arrowheads depict more restricted zones of mitophagy within tubules. Bar, 50 µm. (C) Representative Airyscan images from LAMP1 immunostained adult *mito*-QC kidney sections. Arrows highlight lysosomes containing degraded mitochondria. Bar, 5 µm. (D) Image showing adult *mito*-QC kidney sections immunolabeled with antibodies to the DCT marker, NCC. NCC-positive DCTs are demarcated by dashed lines, whereas arrows highlight NCC-immunonegative PCTs exhibiting pronounced apical mitophagy. DAPI is shown in blue. Bar, 20 µm. (E) Sample semiquantitative analysis of mitophagy in renal cortical tubules of *mito*-QC adult littermate kidneys. Data represent mean number of total and NCC-positive mitolysosomes, generated from a single kidney from two individual animals, with 15 fields analyzed per animal. Data from these kidneys were also used for Fig. 5 D.

mitophagy in the E17.5 cortical tubular system occurs at a much lower rate (compare Fig. 6 A with Fig. 7, A–C). Additionally, we observe an increased level of mCherry-only puncta in embryonic glomeruli rather than in the cortical tubules. This is in stark contrast to renal mitophagy in the adult, where cortical tubules exhibit a greater degree of mitophagy compared with their associated glomeruli (Fig. 7 D). We also assessed the early kidney in cryosections from E14.5 reporter embryos but were unable to detect any robust level of mitophagy that resembled our observations in the late-embryonic or adult kidney (unpublished data). These data demonstrate that renal mitophagy is spatially regulated, in a developmentally-dependent fashion.

Discussion

Using *mito*-QC to reveal mitochondrial cell biology in vivo

We sought to demonstrate the potential of *mito*-QC as an unrivalled tool to simultaneously resolve mitochondrial turnover

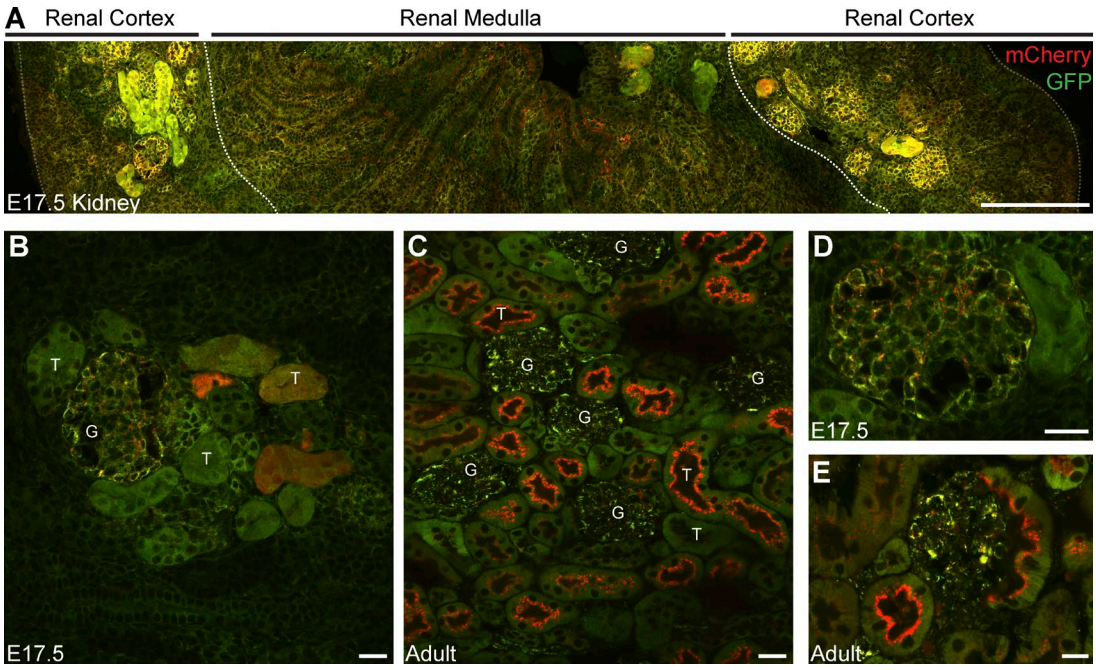

Figure 7. **Spatiotemporal regulation of renal mitophagy.** (A) Tile scan showing a parasagittal view of a representative embryonic kidney from an E17.5 *mito*-QC reporter embryo. Dashed lines demarcate macroanatomical regions of the kidney. Bar, 200 µm. (B and C) Representative image of renal cortex from sections of E17.5 and adult kidney. G, glomerulus; T, tubule. Magnified view of glomeruli from (D) embryonic and (E) adult kidney. Bars, 20 µm.

and network architecture within specific cellular subsets in vivo. Even so, using this model, we have uncovered previously unknown biology pertaining to mitophagy and mitochondrial organization in different organ systems, at different stages of mammalian life. Our findings pave the way for future studies to build on their mechanistic and physiological significance. Our research using *mito*-QC demonstrates the spatially restricted nature of mitophagy as a process within distinct cellular subtypes. Furthermore, our findings provoke a reassessment of how mitophagy is viewed as simply a protective response to mitotoxic damage or that it only occurs in specific physiological contexts such as reticulocyte development (Schweers et al., 2007; Mortensen et al., 2010; Novak et al., 2010). During the preparation of this manuscript, Sun et al. (2015) published a mitophagy reporter mouse that expresses a mitochondrial-matrix targeted fluorescent protein, termed mt-Keima, that has different fluorescent properties at acidic and neutral pH. Conceptually, both *mito*-QC and mt-Keima seem similar, as the principle of detecting mitophagy in tissues relies on a change in pH. However, because of the physicochemical characteristics of Keima, we believe that *mito*-QC affords superior versatility with a more binary-based readout of mitophagy. During this pH change, the Keima protein undergoes a gradual shift in fluorescence excitation, with an overlap in the emission spectra. As Sun et al. (2015) outline in the limitations of their model, this spectral overlap can complicate the interpretation of mitophagy in tissue because the distinction between acidic and neutral environments is not always obvious and likely influenced by tissue processing. Moreover, this ambiguity in the interpretation of mitophagy using the mt-Keima mouse is compounded by the fact that the Keima signal is lost upon conventional fixation, as is stated in the original paper describing this protein (Katayama et al., 2011). Analyses with the mt-Keima mouse model require tissue to be freshly sectioned and visualized immediately. As routine or specialized immunochemical analyses are dependent on tissue fixation, it is therefore infeasible to simultaneously detect mitophagy in immunolabeled cellular populations of interest in tissues derived from the mt-Keima model. In terms of identifying specific cell populations within tissues, this drawback restricts researchers to making regional assumptions that rely on classic anatomical landmarks, many of which require specialist expertise to identify with confidence and are more open to interpretation. It is important to note that complex tissues often exhibit a high degree of cellular heterogeneity and variability, which is only apparent when labeled with markers for particular cellular subtypes in vivo. Although the mt-Keima mouse is undoubtedly a powerful model, *mito*-QC overcomes these limitations and represents an unrivalled and experimentally advantageous tool that can unequivocally resolve multiple aspects of mitochondrial cell biology in vivo at an unprecedented cellular resolution.

mito-QC offers researchers superior utility and flexibility for several experimentally demonstrable reasons: (1) Unlike preexisting models, *mito*-QC *is* the only model that facilitates the simultaneous detection of vertebrate mitophagy and mitochondrial architecture, because of the unique OMM-localization of the reporter construct. (2) Furthermore, unlike mt-Keima, *mito*-QC's tractability is underscored by its compatibility with classical techniques in immunohistochemistry and contemporary advances in whole-tissue imaging, which enables the subsequent assessment of mitophagy and mitochondrial networks within distinct cellular subtypes and whole organs. (3) Mitochondrial networks and mitolysosomes are easily viewed in *mito*-QC without any need for an advanced microscopy setup. Although recent developments in microscopy have improved the sensitivity of confocal microscopy through the incorporation of advanced detectors (Airyscan), we routinely used conventional laser scanning confocal microscopy throughout this study. We hope that this aspect of *mito*-QC will be an accessible and powerful tool to those in the wider scientific community where

resources may be limited. (4) The end-point readout of *mito*-QC is unambiguous because of the distinct emission and excitation spectra of GFP and mCherry. Unlike mt-Keima where it may be difficult to conclusively delineate a positive mitophagy-reporter signal because of overlapping spectra and background, *mito*-QC enables researchers to decisively detect and quantitate mitophagy in vivo with confidence. For these aforementioned reasons, we think this distinct tractability of *mito*-QC confers a significant advantage to researchers interested in various areas of mammalian mitochondrial biology.

We believe that the utility of the *mito*-QC model is only restricted by three minor limiting factors:

(1) Histological considerations of the *mito*-QC reporter. As we have previously published in our cell-based assays, the pH of fixative used is a critical factor when using *mito*-QC, to maintain the lysosomal quenching of the GFP signal. A fixative with pH of 7.0 ensures consistency in cell-based and histological-based readouts of mitophagy with *mito*-QC. We advise researchers to follow our optimized methods for reliable and reproducible results. It is also important to note that we have found that traditional heat-mediated antigen-retrieval (AR) techniques are incompatible with *mito*-QC fluorescence. Ultimately, a limited number of antibody reagents that depend on AR may be precluded from use with *mito*-QC; thus, we advise researchers to use thin cryosections in combination with optimized immunodetection protocols for each antibody to ensure best results. Interestingly, we have found that a classical SDS-mediated AR method does not perturb the reporter signal, and this may be a suitable option to test with antibody reagents that are likely to require AR (Brown et al., 1996). Regarding whole-mount histochemistry, we have tested a limited number of *mito*-QC tissues (brain, heart, and kidneys) using the iDISCO protocol. In whole kidney and heart tissues, we were able to resolve mitochondria and mitolysosomes without immunolabeling; however, it should be noted that we observed some de-quenching of the GFP signal in optically cleared whole-tissue specimens. This is likely caused by the harsh solvents and reagents used in this procedure. Nonetheless, this was not sufficient to obstruct visualization of mitolysosomes or mitochondria within the tissues we assessed. Future optimization and iterations of the protocol for individual *mito*-QC tissues will most likely resolve these issues. Researchers should note that it may prove problematic to resolve individual mitochondria in tissues with a dense mitochondrial network using whole-mount approaches; however, the visualization of mitolysosomes may prove more feasible. We would advise researchers to use trimmed tissue blocks or slices to reduce incubation times in clearing solutions that may perturb the emission properties of the reporter.

(2) Restricted availability in fluorophore selection for triple immunolabeling. As *mito*-QC already relies on two primary endogenous fluorophores (GFP and mCherry) for its detection, users are restricted to selecting the blue (405) or far-red emission spectra (633–647 nm) to detect additional fluorescent labels. In this study, we selected DAPI as a nuclear counterstain to reveal tissue architecture for most experiments. Though this is not necessarily a limitation per se, inadequate optimization of histological and secondary detection parameters may result in potential artifacts (e.g., bleed-through of far red–positive structures into the red channel). With sufficient optimization, we have found that this limitation is easily resolved.

(3) As *mito*-QC is dependent on correct localization of the reporter to the outer mitochondrial membrane, it is conceivable that certain (as yet unknown) conditions could disrupt this biological process and affect assay reliability. It is important to note that we have found no evidence for this, but additional experiments such as the EM used here would rule this out when confirming new and unexpected instances of mitophagy.

Our findings using *mito*-QC have unearthed regions of unexpected yet pronounced physiological mitophagy in mammals. One striking example is the discovery of a high rate of mitophagy in kidney PCTs. Although the high energetic demand of PCTs is well established, the dramatic mitochondrial turnover described here was completely unsuspected, because previous studies revealed that under steady-state conditions, general autophagy proceeds but does not appear to be elevated (Li et al., 2014). This highlights the complex and selective nature of autophagy within distinct cellular subtypes of a given tissue. As mitochondrial dysfunction has been implicated in both chronic and acute kidney diseases (Emma et al., 2016), our data also lend experimental credence to the idea that aberrant mitophagy could be a critical process in renal pathophysiology.

Mitochondria have granted the Eukarya a survival advantage throughout evolution; however, it has emerged that their dysfunction confers a devastating vulnerability to mammalian cells. Future pharmacological and genetic studies using *mito*-QC will be essential to fully decipher the contribution of mitochondrial turnover and morphology to a variety of organ systems during development and disease. The mechanistic elaboration of cell-specific mitophagy pathways may also help in evaluating their potential as therapeutic targets for the treatment of a variety of human diseases, particularly those linked to mitochondrial dysfunction. Ultimately, we hope that our end-point *mito*-QC model will underpin prospective work that unravels the physiological relevance of distinct mitochondrial turnover pathways in vivo.

Materials and methods

Generation of mitophagy reporter mice

mito-QC mice were based on a strategy (constitutive knockin of mCherry-GFP-mtFIS1$^{101–153}$) described by Allen et al. (2013) and generated using targeted transgenesis by TaconicArtemis GmbH. Recombination-mediated cassette exchange (RMCE) was used to insert a CAG promoter cassette and the open reading frame for the mCherry-GFP-FIS1 fusion protein including a Kozak sequence (GCCACC) into the mouse *Rosa26* locus. The RMCE vector was transfected into a TaconicArtemis C57BL/6 ES cell line containing RMCE docking sites in the *Rosa26* locus. Recombinant clones were isolated via positive–negative (Neo^R) selection. Mice were maintained on a C57BL/6 background. Genotyping was performed by diagnostic end-point PCR using genomic DNA isolated from tissue biopsy specimens with the following sets of forward and reverse primers: set 1, 5′-CAAAGACCC CAACGAGAAGC-3′ and 5′-CCCAAGGCACACAAAAAACC-3′; and set 2, 5′-CTCTTCCCTCGTGATCTGCAACTCC-3′ and 5′-CAT GTCTTTAATCTACCTCGATGG-3′. These were used to detect WT and knockin alleles using KOD Hot Start DNA polymerase (EMD Millipore) and manufacturer-recommended conditions. All animal studies and breeding was approved by the University of Dundee ethical review committee and performed under a UK Home Office project license, in accordance with the Animal Scientific Procedures Act of 1986.

Primary cell culture

For experiments using MEFs, embryos were derived from time-mated pregnant females at E12 and staged according to the criteria of Theiler

(1989). E12 embryos were decapitated and eviscerated, and MEFs and adult fibroblasts were generated using standard protocols, cultured in DMEM/20% FBS/penicillin-streptomycin at 37°C/5% CO_2.

Immunocytochemistry

For immunocytochemical and fluorescence microscopy, primary MEFs were cultured on glass coverslips or glass-bottom dishes (Greiner) processed as described previously (Allen et al., 2013) in DMEM/20% FBS/nonessential amino acids/L-glutamate and penicillin-streptomycin at 37°C/5% CO_2. To facilitate comparative microscopic analyses of littermate WT and reporter MEFs in the same dish, mixed cultures were also established. Specifically, cells were fixed for 15 min at room temperature using 3.7% formaldehyde and 200 mM Hepes, pH 7.0. After fixation, samples were washed in PBS and blocked and permeabilized with 1% donkey serum in PBS containing 0.2% Triton X-100 (blocking solution) for 30 min at RT. Primary antibodies were incubated in the blocking solution for 1 h at room temperature or overnight at 4C with gentle agitation. After washing in PBS, samples were incubated with the appropriate Alexa Fluor secondary antibody for 1 h at RT in the dark, with either a 406- or 633-nm fluorochrome conjugate. After washing steps and nuclear counterstaining with DAPI (in instances where 633 antibodies were used), labeled cells were mounted using Vectashield and sealed with nail polish.

MitoTracker staining and live imaging of cultured MEFs

MEFs were seeded in glass-bottom quadrant dishes (Greiner) and incubated at 37°C/5% CO_2 in culture medium (DMEM/20% FBS/1× non-essential amino acids/penicillin-streptomycin) containing 200 nM MitoTracker Deep Red FM for 30 min. The MEFs were imaged via time-lapse confocal microscopy and imaged on a ZEISS LSM 700 with stage incubator maintained at 37°C and 5% CO_2 using a Zeiss Plan-Neofluar 40× objective (NA 1.30).

Immunohistochemistry

For studies investigating mitophagy in vivo, adult mice were terminally anesthetized and trans-cardially perfused with PBS before perfusion with freshly made, sterile-filtered 3.7% (wt/vol) PFA in 200 mM Hepes buffer, pH 7.0. Organs of interest were excised and postfixed via immersion fixation (~20× tissue volume) in PFA for 8–12 h at 4°C. For studies investigating developmental mitophagy, time-mated pregnant females were humanely euthanized and embryos were extracted and staged according to the criteria of Theiler (1989). After decapitation and brief exsanguination, embryos were briefly rinsed in cold 1× PBS and immersion fixed for 2–6 h at 4°C, according to developmental stage. For some studies, organs of interest were excised from fixed embryos before further histochemical processing. Fixed tissues were washed extensively in 1× PBS at 4°C, before density-dependent cryoprotection in filtered 30% (wt/vol) sucrose/PBS at 4°C. Cryoprotected tissues were oriented in Peel-A-Way molds (Ted Pella Inc.), embedded in OCT (Sakura; Thermo Fisher Scientific), and slowly frozen via controlled immersion in chilled isopentane on dry ice and sectioned on a cryostat (CM3050S; Leica Biosystems). Tissue sections were mounted directly to Leica Biosystem SurgiPath *Xtra*-adhesive slides before processing for immunolabeling or tinctorial staining. For immunohistochemical detection of markers of interest, tissue sections were rehydrated and washed with 1× PBS, before blocking and incubation steps in 1–5% BSA containing 0.3–0.8% Triton X-100, depending on the particular primary antibody. For staining with monoclonal antibodies, sections were blocked with M.O.M (Mouse-on-Mouse blocking serum as per the manufacturers instructions; Vector Laboratories). Tissue sections were washed in PBS before incubation with fluorophore-conjugated secondary antibodies (1:500 Alexa Fluor 405, 488, 594, and 633; Thermo Fisher Scientific) for 1 h at RT. After washes in 1× PBS, sections were counterstained with DAPI (1:1,000; Thermo Fisher Scientific). Immunolabeled sections were washed and mounted using Vectashield (Vector Laboratories). Images were acquired using a LSM700 laser-scanning confocal microscope (ZEISS; Plan-Neofuar ×40 objective, NA 1.30 or α-Plan Apochromat ×100 objective, NA 1.46), LSM 710 Multiphoton (Plan-Neofuar ×40 objective, NA 1.30; Plan Apochromat ×63 objective NA 1.4; Plan Apochromat ×20 objective, NA 0.8), or a LSM880 Airyscan microscope (ZEISS; Plan Apochromat ×63 objective, NA 1.4) and processed using ZEISS Zen Software/Adobe Photoshop. Images were digitally altered within linear parameters, with minimal adjustments to levels and linear contrast applied to all images. The following primary antibodies were used in this study: rat anti-LAMP1 and rabbit anti-TOM20 (Santa Cruz Biotechnology, Inc.); rabbit anti–cleaved caspase-3 (Cell Signaling Technology); rabbit anti-Ki67, chicken anti-GFP, and mouse anti-RFP (Abcam); mouse anticalbindin (Swant); anti-GFP (Aves); anti-mCherry (Thermo Fisher Scientific); anti-RFP (Rockland); rabbit anti-PMP70 (Sigma-Aldrich); and sheep anti-NCC (residues 906–925 of human NCC, S965B; https://mrcppureagents.dundee.ac.uk).

Whole-mount immunohistochemistry using iDISCO

For labeling of mitochondria and mitophagosomes in excised cerebella, we used the same immunolabeling protocol as referred to in the original iDISCO publication (Renier et al., 2014). For some kidney and heart specimens, we proceeded immediately to the solvent-based clearing steps after fixation. Cleared tissue preparations were imaged on the LSM 710 MP with a multiphoton laser and ZEISS Plan-Apochromat 20× objective (NA 0.8).

Semiautomated quantitation

Images were processed with Volocity 3D Image Analysis Software (PerkinElmer) using algorithms developed to analyze object overlap and count individual structures. For all analyses, we obtained images using uniform random sampling by an experimenter blind to all conditions. All images in each experimental group were processed as a batch using identical protocols.

To assess the degree of overlap between LAMP1 and mCherry-only staining in Volocity, (1) LAMP1-positive structures (identified in far red/Alexa Fluor 633) were found using the "Find Objects/Automatic Method" in Otsu's method (Otsu, 1979); (2) mCherry-only puncta were found using the same method, but with a threshold offset of 110 to select *bona-fide* bright structures; and (3) mCherry-positive structures were intersected with LAMP1-positive structures.

For counting the density of mCherry structures in tissue sections with Volocity, (1) mCherry-positive structures were found using the Automatic method but using an offset of 110 to select only the brightest structures; (2) GFP-positive bright structures were found using the Automatic setting, offset by 110 as for mCherry; (3) mCherry-positive objects that were also GFP positive were excluded from the count using the "Exclude touching objects" command; (4) and counts were expressed as a ratio of the total area of tissue, because some section images did not completely fill the field of view. This was calculated using the "Find objects" command using intensities −1 standard deviation from the mean intensity.

To assess the degree of mitophagy in NCC-positive DCTs, we followed a similar protocol: (1) mCherry-positive structures were found using the Automatic method but using an offset of 110 to select only the brightest structures; (2) GFP-positive bright structures were found using the Automatic setting, offset by 110 as for the mCherry; (3) NCC-positive structures were also found in the Alexa633 channel using the Automatic method; and (4) overlapping objects were then found and expressed as a percentage of the total number of red structures.

Statistical analysis

For statistical analyses, Student's *t* test was used for pairwise comparisons, whereas multiple comparisons were analyzed with one-way analysis of variance and Tukey's post hoc test where indicated.

Preparation of mouse tissue lysates and immunoblotting

Mouse tissues were rapidly excised, snap frozen in liquid nitrogen and stored at −80°C. Subsequently, tissues were homogenized on ice using a Kinematica Polytron, in a 10-fold mass excess of ice-cold lysis buffer containing 50 mM Tris/HCl, pH 7.5, 1 mM EDTA, 1 mM EGTA, 1% Triton X-100, 1 mM sodium orthovanadate, 50 mM NaF, 5 mM sodium pyrophosphate, 0.27 M sucrose, and Complete protease inhibitor cocktail (Roche). Lysates were clarified by centrifugation at 13,000 *g* for 30 min at 4°C. Supernatants were carefully removed, snap-frozen and stored at −80°C. 20–30 µg of denatured protein lysates were resolved by SDS-PAGE using precast 4–12% Novex Bis-Acrylamide gels (Thermo Fisher Scientific). Gels were electrotransfered to nitrocellulose (GE Healthcare) using a Bio-Rad Transblot Transfer Apparatus. Equal loading was evaluated by staining membranes with the reversible protein-binding dye, Ponceau-S (Sigma-Aldrich). Membranes were incubated with primary antibodies overnight at 4°C in 5% (wt/vol) nonfat dry milk (Marvel) diluted in TBST (Tris-buffered saline with 0.1% Tween-20). After washes in TBST, secondary detection was performed with HRP-conjugated Protein G (1:1,000; EMD Millipore) for 1 h at room temperature as described previously (Allen et al., 2013). Membranes were washed in TBST and developed using standard chemiluminescence with ECL and exposure to hyperfilm (GE Healthcare).

Electron microscopy

Immunogold labeling on frozen hydrated sections was performed as described previously (Tokuyasu, 1973). Tissue was infiltrated with 2.4 M sucrose in PBS overnight, frozen in liquid nitrogen, and sectioned on a Leica UCT ultramicrotome with EMFCS cold box (Leica Biosystems). GFP was localized using rabbit anti-GFP antibody (A11122; Molecular Probes) and secondary gold-conjugated goat anti–rabbit IgG (BBI). For conventional transmission EM, tissue was perfusion fixed in 4% formaldehyde and 2.5% gluteraldehyde in 0.2 M sodium cacodylate buffer, followed by dehydration in alcohol series, and then embedded in Durcupan resin (Perng et al., 2004). Sections taken on the Leica UCT ultramicrotome were contrasted with uranyl acetate and lead citrate. Sections were examined on a Jeol 1200 EX electron microscope (Jeol) and images taken on SIS Megaview III camera (EMSIS).

Assessment of mitochondrial function

Oxygen consumption was measured using a Seahorse XF24 Extracellular Flux analyser (Seahorse Bioscience). Cells were cultured in 24-well Seahorse plates at a density of 5×10^4 cells per well. Cell culture medium was replaced with unbuffered DMEM containing 200 mM GlutaMax-1, 100 mM sodium pyruvate, 25 mM glucose, 32 mM NaCl, and 40 M phenol red. Oxygen consumption was measured and respiration rate analyzed with injections of 1 µM oligomycin, 1 µM FCCP, and 10 µM antimycin A as previously described (Allen et al., 2013). Results were normalized to total protein determined using Bradford assay.

Citrate synthase activity measurements

Citrate synthase activity was determined as previously (Allen et al., 2013). In brief, cell lysates were incubated with 100 mM Tris, pH 8.0, 0.1% Triton X-100, 0.1 mM acetyl-coenzyme A, and 0.2 mM DTNB (5′-dithio-bis (2-nitrobenzoic acid)). Reactions were started with 0.2 mM oxaloacetate, and the reaction was measured at 405 nm for 1.5 min at 10-s intervals at 30°C using a VersaMAX plate reader (Molecular Devices). All reagents were purchased from Sigma-Aldrich.

Online supplemental material

Fig. S1 shows in vitro characterization of *mito*-QC. Fig. S2 shows that *mito*-QC indicates delivery of mitochondrial to autolysosomes and staining in general is distinct from peroxisomal staining. Fig. S3 shows that GFP-immunolabeling is highly specific for mitochondria as visualized by electron microscopy. Fig. S4 shows a comparative assessment of cardiac mitochondrial morphology and mitophagy in wild-type and reporter mice. Fig. S5 shows that *mito*-QC is compatible with contemporary techniques in histochemistry and whole-tissue imaging. Video 1 shows mitochondrial dynamics in wild-type and *mito*-QC MEFs. Video 2 shows mitochondrial architecture in the cerebellum. Video 3 shows mitochondria and mitophagy in the renal cortex. Online supplemental material is available at http://www.jcb.org/cgi/content/full/jcb.201603039/DC1. Additional data are available in the JCB DataViewer at http://dx.doi.org/10.1083/jcb.201603039.dv.

Acknowledgments

We thank our departmental support teams for their assistance (Medical Research Council Genotyping and Tissue Culture teams) and the School of Life Sciences Biological Services (all resource units) for the essential management, maintenance, and husbandry of mice. Thanks also to Ngaire Dennison for valuable advice on mouse studies and Tim Cummins for assistance and guidance in performing Seahorse assays. We thank John Rouse and Catherine Rodger for critical reading of the manuscript. We also thank Kevin O'Shaughnessy (University of Cambridge) for help with renal physiology.

We also acknowledge the pharmaceutical companies supporting the Division of Signal Transduction Therapy Unit (AstraZeneca, Boehringer-Ingelheim, GlaxoSmithKline, Merck KGaA, Janssen Pharmaceutica, and Pfizer) for financial support. This work was funded by Medical Research Council grant MC_UU_12016/4 to I.G. Ganley and a Wellcome Trust Senior Research Fellowship in Clinical Science (101022/Z/13/Z) to M.M.K. Muqit.

The authors declare no additional competing financial interests.

Submitted: 10 March 2016
Accepted: 6 July 2016

References

Airik, R., and A. Kispert. 2007. Down the tube of obstructive nephropathies: the importance of tissue interactions during ureter development. *Kidney Int.* 72:1459–1467. http://dx.doi.org/10.1038/sj.ki.5002589

Allen, G.F., R. Toth, J. James, and I.G. Ganley. 2013. Loss of iron triggers PINK1/Parkin-independent mitophagy. *EMBO Rep.* 14:1127–1135. http://dx.doi.org/10.1038/embor.2013.168

Barbosky, L., D.K. Lawrence, G. Karunamuni, J.C. Wikenheiser, Y.Q. Doughman, R.P. Visconti, J.B. Burch, and M. Watanabe. 2006. Apoptosis in the developing mouse heart. *Dev. Dyn.* 235:2592–2602. http://dx.doi.org/10.1002/dvdy.20885

Bingol, B., J.S. Tea, L. Phu, M. Reichelt, C.E. Bakalarski, Q. Song, O. Foreman, D.S. Kirkpatrick, and M. Sheng. 2014. The mitochondrial deubiquitinase USP30 opposes parkin-mediated mitophagy. *Nature.* 510:370–375. http://dx.doi.org/10.1038/nature13418

Brown, D., J. Lydon, M. McLaughlin, A. Stuart-Tilley, R. Tyszkowski, and S. Alper. 1996. Antigen retrieval in cryostat tissue sections and cultured cells by treatment with sodium dodecyl sulfate (SDS). *Histochem. Cell Biol.* 105:261–267. http://dx.doi.org/10.1007/BF01463929

Burté, F., V. Carelli, P.F. Chinnery, and P. Yu-Wai-Man. 2015. Disturbed mitochondrial dynamics and neurodegenerative disorders. *Nat. Rev. Neurol.* 11:11–24. http://dx.doi.org/10.1038/nrneurol.2014.228

Carelli, V., and D.C. Chan. 2014. Mitochondrial DNA: impacting central and peripheral nervous systems. *Neuron.* 84:1126–1142. http://dx.doi.org/10.1016/j.neuron.2014.11.022

Celio, M.R. 1990. Calbindin D-28k and parvalbumin in the rat nervous system. *Neuroscience.* 35:375–475. http://dx.doi.org/10.1016/0306-4522(90)90091-H

Chresta, C.M., B.R. Davies, I. Hickson, T. Harding, S. Cosulich, S.E. Critchlow, J.P. Vincent, R. Ellston, D. Jones, P. Sini, et al. 2010. AZD8055 is a potent, selective, and orally bioavailable ATP-competitive mammalian target of rapamycin kinase inhibitor with in vitro and in vivo antitumor activity. *Cancer Res.* 70:288–298. http://dx.doi.org/10.1158/0008-5472.CAN-09-1751

Dorn, G.W. II, R.B. Vega, and D.P. Kelly. 2015. Mitochondrial biogenesis and dynamics in the developing and diseased heart. *Genes Dev.* 29:1981–1991. http://dx.doi.org/10.1101/gad.269894.115

Dørup, J. 1985. Ultrastructure of distal nephron cells in rat renal cortex. *J. Ultrastruct. Res.* 92:101–118. http://dx.doi.org/10.1016/0889-1605(85)90132-6

Eirin, A., A. Lerman, and L.O. Lerman. 2015. Mitochondria: a pathogenic paradigm in hypertensive renal disease. *Hypertension.* 65:264–270. http://dx.doi.org/10.1161/HYPERTENSIONAHA.114.04598

Emma, F., G. Montini, S.M. Parikh, and L. Salviati. 2016. Mitochondrial dysfunction in inherited renal disease and acute kidney injury. *Nat. Rev. Nephrol.* 12:267–280. http://dx.doi.org/10.1038/nrneph.2015.214

Fougeray, S., and N. Pallet. 2015. Mechanisms and biological functions of autophagy in diseased and ageing kidneys. *Nat. Rev. Nephrol.* 11:34–45. http://dx.doi.org/10.1038/nrneph.2014.201

Glancy, B., L.M. Hartnell, D. Malide, Z.X. Yu, C.A. Combs, P.S. Connelly, S. Subramaniam, and R.S. Balaban. 2015. Mitochondrial reticulum for cellular energy distribution in muscle. *Nature.* 523:617–620. http://dx.doi.org/10.1038/nature14614

Gong, G., M. Song, G. Csordas, D.P. Kelly, S.J. Matkovich, and G.W. Dorn II. 2015. Parkin-mediated mitophagy directs perinatal cardiac metabolic maturation in mice. *Science.* 350:aad2459. http://dx.doi.org/10.1126/science.aad2459

Hailey, D.W., A.S. Rambold, P. Satpute-Krishnan, K. Mitra, R. Sougrat, P.K. Kim, and J. Lippincott-Schwartz. 2010. Mitochondria supply membranes for autophagosome biogenesis during starvation. *Cell.* 141:656–667. http://dx.doi.org/10.1016/j.cell.2010.04.009

Hamasaki, M., N. Furuta, A. Matsuda, A. Nezu, A. Yamamoto, N. Fujita, H. Oomori, T. Noda, T. Haraguchi, Y. Hiraoka, et al. 2013. Autophagosomes form at ER-mitochondria contact sites. *Nature.* 495:389–393. http://dx.doi.org/10.1038/nature11910

Higgins, G.C., and M.T. Coughlan. 2014. Mitochondrial dysfunction and mitophagy: the beginning and end to diabetic nephropathy? *Br. J. Pharmacol.* 171:1917–1942. http://dx.doi.org/10.1111/bph.12503

Katayama, H., T. Kogure, N. Mizushima, T. Yoshimori, and A. Miyawaki. 2011. A sensitive and quantitative technique for detecting autophagic events based on lysosomal delivery. *Chem. Biol.* 18:1042–1052. http://dx.doi.org/10.1016/j.chembiol.2011.05.013

Klionsky, D.J., K. Abdelmohsen, A. Abe, M.J. Abedin, H. Abeliovich, A. Acevedo Arozena, H. Adachi, C.M. Adams, P.D. Adams, K. Adeli, et al. 2016. Guidelines for the use and interpretation of assays for monitoring autophagy (3rd edition). *Autophagy*. 12:1–222. http://dx.doi.org/10.1080/15548627.2015.1100356

Koch, A., Y. Yoon, N.A. Bonekamp, M.A. McNiven, and M. Schrader. 2005. A role for Fis1 in both mitochondrial and peroxisomal fission in mammalian cells. *Mol. Biol. Cell.* 16:5077–5086. http://dx.doi.org/10.1091/mbc.E05-02-0159

Kutuzov, H., and H. Sicher. 1953. Comparative anatomy of the mucosa of the tongue and the palate of the laboratory mouse. *Anat. Rec.* 116:409–425. http://dx.doi.org/10.1002/ar.1091160403

Leto, K., M. Arancillo, E.B. Becker, A. Buffo, C. Chiang, B. Ding, W.B. Dobyns, I. Dusart, P. Haldipur, M.E. Hatten, et al. 2015. Consensus Paper: Cerebellar Development. *Cerebellum.* http://dx.doi.org/10.1007/s12311-015-0724-2

Li, L., Z.V. Wang, J.A. Hill, and F. Lin. 2014. New autophagy reporter mice reveal dynamics of proximal tubular autophagy. *J. Am. Soc. Nephrol.* 25:305–315. http://dx.doi.org/10.1681/ASN.2013040374

Mortensen, M., D.J. Ferguson, M. Edelmann, B. Kessler, K.J. Morten, M. Komatsu, and A.K. Simon. 2010. Loss of autophagy in erythroid cells leads to defective removal of mitochondria and severe anemia in vivo. *Proc. Natl. Acad. Sci. USA.* 107:832–837. http://dx.doi.org/10.1073/pnas.0913170107

Novak, I., V. Kirkin, D.G. McEwan, J. Zhang, P. Wild, A. Rozenknop, V. Rogov, F. Löhr, D. Popovic, A. Occhipinti, et al. 2010. Nix is a selective autophagy receptor for mitochondrial clearance. *EMBO Rep.* 11:45–51. http://dx.doi.org/10.1038/embor.2009.256

Nunnari, J., and A. Suomalainen. 2012. Mitochondria: in sickness and in health. *Cell.* 148:1145–1159. http://dx.doi.org/10.1016/j.cell.2012.02.035

Otsu, N. 1979. Threshold selection method from Gray-level histograms. *IEEE Trans Syst Man Cybern Syst.* 9:62–66. http://dx.doi.org/10.1109/TSMC.1979.4310076

Perng, M.D., A. Sandilands, J. Kuszak, R. Dahm, A. Wegener, A.R. Prescott, and R.A. Quinlan. 2004. The intermediate filament systems in the eye lens. *Methods Cell Biol.* 78:597–624. http://dx.doi.org/10.1016/S0091-679X(04)78021-8

Rajendran, R., and S. Sivapathasundharam. 2009. Shafer's Textbook of Oral Pathology. Sixth edition. Elsevier, India. 963 pp.

Renier, N., Z. Wu, D.J. Simon, J. Yang, P. Ariel, and M. Tessier-Lavigne. 2014. iDISCO: a simple, rapid method to immunolabel large tissue samples for volume imaging. *Cell.* 159:896–910. http://dx.doi.org/10.1016/j.cell.2014.10.010

Sandborn, E. 1972. Light and Electron Microscopy of Cells and Tissues. Academic Press, New York, London. 217 pp.

Schweers, R.L., J. Zhang, M.S. Randall, M.R. Loyd, W. Li, F.C. Dorsey, M. Kundu, J.T. Opferman, J.L. Cleveland, J.L. Miller, and P.A. Ney. 2007. NIX is required for programmed mitochondrial clearance during reticulocyte maturation. *Proc. Natl. Acad. Sci. USA.* 104:19500–19505. http://dx.doi.org/10.1073/pnas.0708818104

Scotti, A.L. 1995. Calbindin D28k in the olivocerebellar projection. A light and electron microscope study. *J. Anat.* 187:649–659.

Soriano, P. 1999. Generalized lacZ expression with the ROSA26 Cre reporter strain. *Nat. Genet.* 21:70–71. http://dx.doi.org/10.1038/5007

Subramanya, A.R., and D.H. Ellison. 2014. Distal convoluted tubule. *Clin. J. Am. Soc. Nephrol.* 9:2147–2163. http://dx.doi.org/10.2215/CJN.05920613

Sun, N., J. Yun, J. Liu, D. Malide, C. Liu, I.I. Rovira, K.M. Holmström, M.M. Fergusson, Y.H. Yoo, C.A. Combs, and T. Finkel. 2015. Measuring in vivo mitophagy. *Mol. Cell.* 60:685–696. http://dx.doi.org/10.1016/j.molcel.2015.10.009

Theiler, K. 1989. The House Mouse: Atlas of Embryonic Development. Springer-Verlag, Heidelberg, Germany. 178 pp.

Tokuyasu, K.T. 1973. A technique for ultracryotomy of cell suspensions and tissues. *J. Cell Biol.* 57:551–565. http://dx.doi.org/10.1083/jcb.57.2.551

Wachstein, M., and E. Meisel. 1955. The distribution of histochemically demonstrable succinic dehydrogenase and of mitochondria in tongue and skeletal muscles. *J. Biophys. Biochem. Cytol.* 1:483–488. http://dx.doi.org/10.1083/jcb.1.6.483

Wang, Y., and S. Hekimi. 2015. Mitochondrial dysfunction and longevity in animals: untangling the knot. *Science.* 350:1204–1207. http://dx.doi.org/10.1126/science.aac4357

Wei, H., L. Liu, and Q. Chen. 2015. Selective removal of mitochondria via mitophagy: distinct pathways for different mitochondrial stresses. *Biochim. Biophys. Acta.* 1853(10, 10 Pt B):2784–2790. http://dx.doi.org/10.1016/j.bbamcr.2015.03.013

Yoshii, S.R., and N. Mizushima. 2015. Autophagy machinery in the context of mammalian mitophagy. *Biochim. Biophys. Acta.* 1853(10, 10 Pt B):2797–2801. http://dx.doi.org/10.1016/j.bbamcr.2015.01.013

Youle, R.J., and D.P. Narendra. 2011. Mechanisms of mitophagy. *Nat. Rev. Mol. Cell Biol.* 12:9–14. http://dx.doi.org/10.1038/nrm3028